Mutual Inductance Calculation of Rectangular Coils at Arbitrary Position With Bilateral Finite Magnetic Shields in Wireless Power Transfer Systems

Zhongbang Chen, Zhongqi Li, *Member, IEEE*, Zhiyuan Lin, Junjun Li, and Yiming Zhang, *Senior Member, IEEE*

***Abstract*—Horizontal or rotational misalignment between the transmitting and receiving coils with magnetic shielding is inevitable during the wireless charging process, which leads to mutual inductance changes between the coils with magnetic shielding. However, there is no literature report on the mutual inductance calculation method for rectangular coils with bilateral finite magnetic shielding at arbitrary position. Therefore, the mutual inductance formulation of the rectangular coil at vertical misalignment is first obtained by the subdomain partition method (SPM). Then, the mutual inductance formulation of the rectangular coil with bilateral finite magnetic shielding at arbitrary position is obtained by the proposed vector coordinate transformation method (VCTM). Finally, this article presents the design of a wireless power transfer system's receiving and transmitting device according to the model of this article. The results of mutual inductance are compared between computational, simulation, and experimental results, and the results show that the mutual inductance error rate is within 4.79%. Moreover, the mutual inductance calculation time is not more than 12 s, which is 11 times faster than the finite element simulation time. The accuracy and rapidity of the proposed method in this article are verified**

***Index Terms*—Magnetic shielding, mutual inductance calculation, rectangular spiral coil, wireless power transfer (WPT).**

I. Introduction

WIRELESS power transfer (WPT) technology can solve endurance problems for electric vehicles [1], [2]. At present, WPT technology is widely used in other fields, such as electronic bio-medicine [3], [4], payment devices [5], [6], drones [7], [8], smart homes [9], etc. WPT system mainly consists of transmitting and receiving coils. However, horizontal and rotational misalignment between the receiving and transmitting coils is unavoidable during the charging process. Therefore, the research on the analytical method of mutual inductance calculation is significant in order to optimize the mutual inductance of the coil structure.

In WPT systems, the most commonly used coil types are rectangular and circular [10], [11], [12], in addition to crosses, polygons, etc. Rectangular coils are widely used because of the large receiving area and the suitability for paved roads. The mutual inductance of the traditional coil model can be obtained by the finite element method (FEM). However, because the FEM is tedious to modify the modeling steps, it is not conducive to closed-loop optimization. In addition, the FEM may have problems such as nonconvergence and a long simulation process. Therefore, scholars have researched several analytical methods to calculate mutual inductance, such as the Newman function [13], the Bessel and Struve functions [14], and the Biot–Savart law [15], [16].

Considerable research has been conducted on calculating the mutual inductance of hollow-core rectangular coils. Cheng and Shu [17], Aydin et al. [18] derived the mutual inductance when rectangular coils are coaxial based on Biot–Savart. However, when the coils are horizontally misaligned, the mutual inductance cannot be calculated. Dehui et al. [19], [20] used the vertex method to obtain the mutual inductance when the coil is misaligned horizontally, but rotational misalignment of the coil cannot be achieved. Altun and Pirinççi [21] derived the arbitrary position mutual inductance of arbitrarily shaped planar polygonal coils based on Stokes' theorem. Wu et al. [22] implemented a method for calculating the mutual inductance of coils under horizontal and rotational misalignment by hyperbolic functions and a spiral factor. However, the magnetic shielding is not considered in the above methods because rectangular coil structures with magnetic shielding are more difficult to math model.

Magnetic shielding materials can be added to the WPT system to improve charging efficiency. There are less research on the calculation of mutual inductance of rectangular coils with magnetic shielding. Luo and Wei [23] proposed a mutual inductance calculation method for horizontally misaligned coil by Maxwell's equations, but only the magnetic shielding on one side of the coil is considered. The above methods are not practical

Manuscript received 26 February 2024; revised 6 June 2024; accepted 5 July 2024. Date of publication 9 July 2024; date of current version 4 September 2024. This work was supported in part by the National Program on Key Research Project under Grant 2022YFB3403200, in part by the Natural Science Foundation of Hunan Province under Grant 2022JJ30226, and in part by the Project supported by the Research Foundation of Education Bureau of Hunan Province under Grant 23A0432. Recommended for publication by Associate Editor A. Safaee. *(Corresponding authors: Zhongqi Li; Yiming Zhang.)*

Zhongbang Chen, Zhiyuan Lin, and Junjun Li are with the College of Traffic Engineering, Hunan University of Technology, Zhuzhou 412007, China (e-mail: m21081101020@stu.hut.edu.cn; m21085400032@stu.hut.edu.cn; lijunjun@hut.edu.cn).

Zhongqi Li is with the College of Traffic Engineering, Hunan University of Technology, Zhuzhou 412007, China, and also with the College of Electrical and Information Engineering, Hunan University, Changsha 410082, China (e-mail: lizhongqi@hnu.edu.cn).

Yiming Zhang is with Fuzhou University, Fuzhou 350002, China (e-mail: zym@fzu.edu.cn).

Color versions of one or more figures in this article are available at https://doi.org/10.1109/TPEL.2024.3425713.

Digital Object Identifier 10.1109/TPEL.2024.3425713

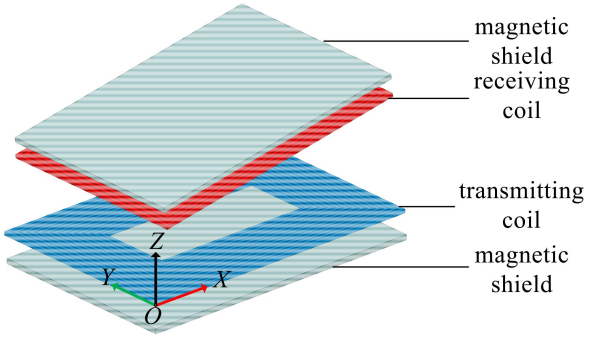

Fig. 1. 3-D diagram of the rectangular coils with bilateral finite magnetic shields at arbitrary position.

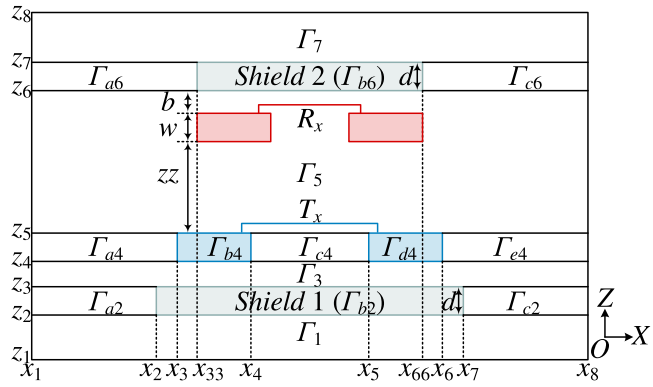

Fig. 2. XZ-plane diagram of the rectangular coils with bilateral finite magnetic shields.

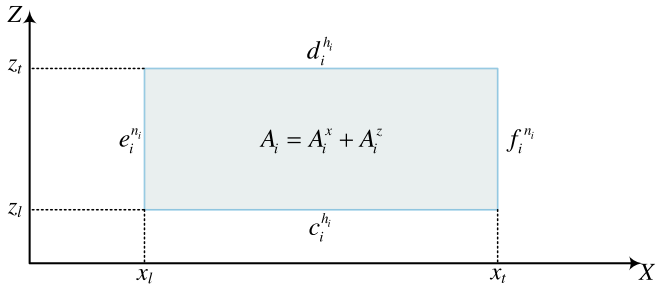

Fig. 3. Schematic diagram of the boundary coordinates of different regions.

because the thickness and width of the magnetic shielding is not considered. Kushwaha et al. [24] derived the mutual inductance of rectangular coils at arbitrary position based on hyperbolic functions and Fourier series expansion. The references is only considered the magnetic shielding of the transmitting coil and not the receiving side. Rituraj et al. [25], Luo et al. [26] derived the mutual inductance of the rectangular coil with bilateral magnetic shields by the separation of variables method. Although the thickness and width of the magnetic shielding are considered in the literature, the calculation of a finite magnetic shielding is achieved. However, these studies failed to calculate the mutual inductance of rectangular coils with bilateral finite magnetic shields at arbitrary position.

In this article, the analytical model for calculating the mutual inductance of rectangular coils with bilateral finite magnetic shields at arbitrary position is shown in Fig. 1. This article presents a new method for the calculation of mutual inductance at arbitrary position, with the following main contributions:

a) The model of rectangular coils with bilateral finite magnetic shields is partitioned using the subdomain partition method (SPM). This method does not require repeated modeling, the procedure computation time is 19 times faster than that of FEM. The runtime of proposed method is 205 times faster than that of literature [25] and 4 times faster than that of literature [26].
b) The mutual inductance of the rectangular coils at arbitrary position of the bilateral finite magnetic shields is calculated by using the vector coordinate transformation method (VCTM). This method can calculate both the horizontal and rotational misalignment of the receiving coil and the magnetic shielding.
c) The proposed method not only achieves a high degree of freedom in the receiving coil, but also has a small error rate in the case of more complex models.

The rest of this article is organized as follows. Section II, a 2-D model of the rectangular coils with bilateral finite magnetic shields is introduced. In Section III, the 2D–3D formulation of the mutual inductance of the coil at arbitrary position is provided. In Section IV, the experiment is discussed. Finally, Section V concludes this article.

II. 2-D Models of Rectangular Coils With Bilateral Finite Magnetic Shields

In this section, an XZ-plane diagram with bilateral finite magnetic shields and rectangular coils is established, as shown in Fig. 2. T_x is the transmitting coil and R_x is the receiving coil. Regions Γ_{b4} and Γ_{d4} are cross-sections of the transmitting coil, and the receiving coil is represented in Fig. 2. Copper material with a relative magnetic permeability of μ_c is used for the coils. Regions Γ_{b2} and Γ_{b6} are magnetic shields, and the rest of the regions are air. The magnetic shielding is made of ferrite with a relative permeability of μ_r and thickness of d. b denotes the air gap between the coil and the magnetic shielding, w denotes the diameter of the single-turn coil, and zz denotes the air gap spacing between the transmitting and receiving coils. The rectangular region $(x_1 < x < x_8, z_1 < z < z_8)$ is the model boundary, i.e., the magnetic vector potential is zero.

A. Magnetic Vector Potential Equation

The excitation current I_p is passed through the transmitting coil. The WPT system operates in the frequency range of 20–100 kHz, so this analytical model is quasi-static. The magnetic vector potential A_i in each region is defined by the Poisson (1). (2) is obtained by the separated variable method, and the specific coordinates of the region boundaries are shown in Fig. 3.

$$\nabla^2 A_i = \frac{\partial^2 A_i}{\partial x^2} + \frac{\partial^2 A_i}{\partial z^2} = -\mu_0 \mu_i J_i \tag{1}$$

$$A_i = A_i^x + A_i^z + A_i^e \tag{2}$$

where, i ($\Gamma_1 \sim \Gamma_7$) denotes the present region, A_i^x is the magnetic vector potential component denoting the z boundary, A_i^z is the magnetic vector potential component denoting the x boundary, and A_i^e denotes the magnetic vector potential due to the current density. $c_i^{h_i}$, $d_i^{h_i}$, $e_i^{n_i}$, $f_i^{n_i}$ are the unknown coefficients. μ_0 denotes the absolute magnetic permeability of the vacuum, μ_i denotes the relative permeability of the region, and J_i denotes the current density.

1) Regions Γ_{b2}, Γ_{b4}, Γ_{d4}, Γ_{b6}

A_i^x and A_i^z of Regions Γ_{b2}, Γ_{b4}, Γ_{d4}, and Γ_{b6} interact on the z-edge (z_l-z_t) and x-edge (x_l-x_t), respectively. According to (2), Regions Γ_{b2}, Γ_{b4}, Γ_{d4}, Γ_{b6} are obtained as follows:

$$A_i^x = (z_t - z)c_i^0 + (z - z_l)d_i^0 + \sum_{h_i=1}^{H_i} \cos(k_{xi}^{h_i}(x - x_l))\cdot \times \left(\frac{c_i^{h_i} \sinh(k_{xi}^{h_i}(z_t - z))}{k_{xi}^{h_i} \sinh(k_{xi}^{h_i} \cdot t_{zi})} + \frac{d_i^{h_i} \sinh(k_{xi}^{h_i}(z - z_l))}{k_{xi}^{h_i} \sinh(k_{xi}^{h_i} \cdot t_{zi})} \right) \tag{3}$$

$$A_i^z = \sum_{n_i=1}^{N_i} \sin(k_{zi}^{n_i}(z - z_l))\cdot \times \left(\frac{e_i^{n_i} \cosh(k_{zi}^{n_i}(x_t - x))}{k_{zi}^{n_i} \sinh(k_{zi}^{n_i} \cdot t_{xi})} - \frac{f_i^{n_i} \cosh(k_{zi}^{n_i}(x - x_l))}{k_{zi}^{n_i} \sinh(k_{zi}^{n_i} \cdot t_{xi})} \right) \tag{4}$$

$$A_i^e = -0.5\mu_0\mu_i J_i z^2. \tag{5}$$

Significantly, the magnetic vector potentials $A_{\Gamma_{b2}}^e = 0$ and $A_{\Gamma_{b6}}^e = 0$ because there is no current in the regions Γ_{b2} and Γ_{b6}. c_i^0, d_i^0, h_i, and n_i are the spatial harmonic numbers. $k_{xi}^{h_i}$ and $k_{zi}^{n_i}$ are the spatial frequencies, and the equations are expressed as follows:

$$\begin{cases} k_{xi}^{h_i} = h_i\pi/t_{xi}, t_{xi} = x_t - x_l \\ k_{zi}^{h_i} = n_i\pi/t_{zi}, t_{zi} = z_t - z_l \end{cases}. \tag{6}$$

2) Regions Γ_{a2}, Γ_{c2}, Γ_{a4}, Γ_{c4}, Γ_{e4}, Γ_{a6}, Γ_{c6}

All these regions are air media, and the region one boundary is in contact with the model boundary. However, since the magnetic vector potential of the model boundary is zero, the expressions of A_i^x and A_i^z for regions Γ_{a2}, Γ_{c2}, Γ_{a4}, Γ_{c4}, Γ_{e4}, Γ_{a6}, and Γ_{c6} can be obtained as follows:

$$A_i^x = \sum_{h_i=1}^{H_i} \sin(k_{xi}^{h_i}(x - x_l))\cdot \times \left(\frac{c_i^{h_i} \sinh(k_{xi}^{h_i}(z_t - z))}{k_{xi}^{h_i} \sinh(k_{xi}^{h_i} \cdot t_{zi})} + \frac{d_i^{h_i} \sinh(k_{xi}^{h_i}(z - z_l))}{k_{xi}^{h_i} \sinh(k_{xi}^{h_i} \cdot t_{zi})} \right) \tag{7}$$

$$A_i^z = \sum_{n_i=1}^{N_i} \sin(k_{zi}^{n_i}(z - z_l))\cdot \times \left(\frac{e_i^{n_i} \sinh(k_{zi}^{n_i}(x_t - x))}{k_{zi}^{n_i} \sinh(k_{zi}^{n_i} \cdot t_{xi})} + \frac{f_i^{n_i} \sinh(k_{zi}^{n_i}(x - x_l))}{k_{zi}^{n_i} \sinh(k_{zi}^{n_i} \cdot t_{xi})} \right). \tag{8}$$

3) Regions Γ_1, Γ_7

Both regions are also air media that are different from other air regions. The two sides of regions Γ_1 and Γ_7 are in contact with the model boundary, so $A_i^z = 0$. A_i^x is continuous with several regions, so the magnetic vector expressions for regions Γ_1 and Γ_7 can be obtained as follows:

$$A_i^x = \sum_{h_i=1}^{H_i} \sin(k_{xi}^{h_i}(x - x_l))\cdot \times \left(-\frac{c_i^{h_i} \sinh(k_{xi}^{h_i}(z_t - z))}{k_{xi}^{h_i} \cosh(k_{xi}^{h_i} \cdot t_{zi})} + \frac{d_i^{h_i} \sinh(k_{xi}^{h_i}(z - z_l))}{k_{xi}^{h_i} \cosh(k_{xi}^{h_i} \cdot t_{zi})} \right). \tag{9}$$

4) Regions Γ_3, Γ_5

Regions Γ_3 and Γ_5 are similar to regions Γ_1 and Γ_7. However, its boundary is not only continuous with the magnetic shielding but also with the transmitting coil. Therefore, the magnetic vector can be expressed as follows:

$$A_i^x = \sum_{h_i=1}^{H_i} \sin(k_{xi}^{h_i}(x - x_l))\cdot \times \left(-\frac{c_i^{h_i} \cosh(k_{xi}^{h_i}(z_t - z))}{k_{xi}^{h_i} \sinh(k_{xi}^{h_i} \cdot t_{zi})} + \frac{d_i^{h_i} \cosh(k_{xi}^{h_i}(z - z_l))}{k_{xi}^{h_i} \sinh(k_{xi}^{h_i} \cdot t_{zi})} \right). \tag{10}$$

B. 2-D Boundary Conditions

The presence of the magnetic shielding will affect the distribution of the magnetic vector potential, which is difficult to describe by differential equations only. Therefore, in order to find a unique solution for the unknown coefficients mentioned in the previous section, different boundary conditions need to be introduced in the math model

$$\begin{cases} B_i = \nabla \times A_i \\ H_i = B_i/(\mu_0\mu_i) \end{cases} \tag{11}$$

$$B_i = \frac{\partial A_i}{\partial z} - \frac{\partial A_i}{\partial x} = B_{xi} + B_{zi}. \tag{12}$$

All regions are divided into the following three cases, as shown in Fig. 4. According to Fig. 4(a), $c_i^{h_i}$ in region Γ_1 and d_i^{hi} in region Γ_7 are zero. The magnetic vector potential at the model boundary is zero. Similarly, $e_i^{n_i}$ in regions Γ_{a2}, Γ_{a4}, and Γ_{a6} are zero according to Fig. 4(b). The $f_i^{n_i}$ in the regions Γ_{c2}, Γ_{e4}, and Γ_{c6} is zero.

C. Solution of Unknown Coefficients

The expressions of the unknown coefficients can be determined by linear equations. The following is an example of region Γ_1. According to Fig. 4(a), the equation for solving the coefficients of region Γ_1 can be found as follows:

$$H_{x\Gamma_1}(x, z_t) = H_{x\Gamma_{a2}}(x_{\Gamma_{a2}}, z_t) + H_{x\Gamma_{b2}}(x_{\Gamma_{b2}}, z_t) + H_{x\Gamma_{c2}}(x_{\Gamma_{c2}}, z_t) \tag{13}$$

where $x_{\Gamma_{a2}} \in (x_1, x_2)$, $x_{\Gamma_{b2}} \in (x_2, x_7)$, $x_{\Gamma_{c2}} \in (x_7, x_8)$.

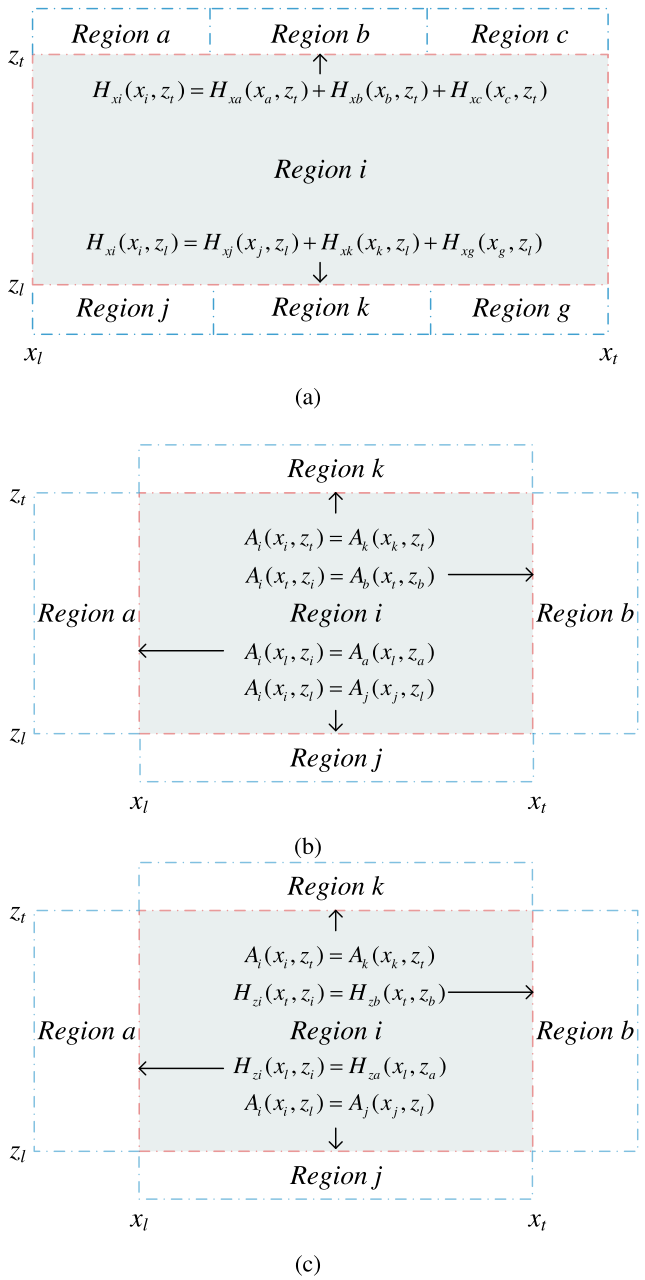

Fig. 4. Diagram of boundary conditions. (a) Regions Γ_1, Γ_3, Γ_5, and Γ_7. (b) Regions Γ_{a2}, Γ_{c2}, Γ_{a4}, Γ_{c4}, Γ_{e4}, Γ_{a6}, and Γ_{c6}. (c) Regions Γ_{b2}, Γ_{b4}, Γ_{d4}, and Γ_{b6}.

Equation (13) is expanded by Fourier series [27], [28], which yields the following expression for the unknown coefficient of Region Γ_1:

$$d_{\Gamma_1}^{h_{\Gamma_1}}=\frac{2\mu_0\mu_{\Gamma_1}}{t_{x\Gamma_1}}\begin{bmatrix}\int_{x_1}^{x_2}H_{x\Gamma_{a2}}(x,z_2)\\+\int_{x_2}^{x_7}H_{x\Gamma_{b2}}(x,z_2)\\+\int_{x_7}^{x_8}H_{x\Gamma_{c2}}(x,z_2)\end{bmatrix}\cdot\sin(k_{x\Gamma_1}^{h_{\Gamma_1}}(x-x_1))dx \tag{14}$$

where $h_{\Gamma_1}=1, 2, 3\ ...H_{\Gamma_1}$.

Similarly, the unknown coefficients of the remaining regional equations can be derived from the different boundary conditions in Fig. 4. Finally, all equations are linked and shown in matrix form as follows:

$$[T]\cdot[S]=[E] \tag{15}$$

where $[T]$ denotes the boundary condition matrix. $[S]$ is the matrix of the unknown coefficients, as shown in (16). $[E]$ is the excitation current matrix, as shown in (17).

$$\begin{aligned}[S]=&\left[\left[d_{\Gamma_1}^{h_{\Gamma_1}}\right]\left[c_{\Gamma_{a2}}^{h_{\Gamma_{a2}}}d_{\Gamma_{a2}}^{h_{\Gamma_{a2}}}f_{\Gamma_{a2}}^{n_{\Gamma_{a2}}}\right]\right.\\&\left[c_{\Gamma_{b2}}^{0}c_{\Gamma_{b2}}^{h_{\Gamma_{b2}}}d_{\Gamma_{b2}}^{0}d_{\Gamma_{b2}}^{h_{\Gamma_{b2}}}e_{\Gamma_{b2}}^{n_{\Gamma_{b2}}}f_{\Gamma_{b2}}^{n_{\Gamma_{b2}}}\right]\left[c_{\Gamma_{c2}}^{h_{\Gamma_{c2}}}d_{\Gamma_{c2}}^{h_{\Gamma_{c2}}}e_{\Gamma_{c2}}^{n_{\Gamma_{c2}}}\right]\\&\left[c_{\Gamma_3}^{h_{\Gamma_3}}d_{\Gamma_3}^{h_{\Gamma_3}}\right]\left[c_{\Gamma_{a4}}^{h_{\Gamma_{a4}}}d_{\Gamma_{a4}}^{h_{\Gamma_{a4}}}f_{\Gamma_{a4}}^{n_{\Gamma_{a4}}}\right]\\&\left[c_{\Gamma_{b4}}^{0}c_{\Gamma_{b4}}^{h_{\Gamma_{b4}}}d_{\Gamma_{b4}}^{0}d_{\Gamma_{b4}}^{h_{\Gamma_{b4}}}e_{\Gamma_{b4}}^{n_{\Gamma_{b4}}}f_{\Gamma_{b4}}^{n_{\Gamma_{b4}}}\right]\left[c_{\Gamma_{c4}}^{h_{\Gamma_{c4}}}d_{\Gamma_{c4}}^{h_{\Gamma_{c4}}}e_{\Gamma_{c4}}^{n_{\Gamma_{c4}}}f_{\Gamma_{c4}}^{n_{\Gamma_{c4}}}\right]\\&\left[c_{\Gamma_{d4}}^{0}c_{\Gamma_{d4}}^{h_{\Gamma_{d4}}}d_{\Gamma_{d4}}^{0}d_{\Gamma_{d4}}^{h_{\Gamma_{d4}}}e_{\Gamma_{d4}}^{n_{\Gamma_{d4}}}f_{\Gamma_{d4}}^{n_{\Gamma_{d4}}}\right]\left[c_{\Gamma_{e4}}^{h_{\Gamma_{e4}}}d_{\Gamma_{e4}}^{h_{\Gamma_{e4}}}e_{\Gamma_{e4}}^{n_{\Gamma_{e4}}}\right]\\&\left[c_{\Gamma_5}^{h_{\Gamma_5}}d_{\Gamma_5}^{h_{\Gamma_5}}\right]\left[c_{\Gamma_{a6}}^{h_{\Gamma_{a6}}}d_{\Gamma_{a6}}^{h_{\Gamma_{a6}}}f_{\Gamma_{a6}}^{n_{\Gamma_{a6}}}\right]\\&\left[c_{\Gamma_{b6}}^{0}c_{\Gamma_{b6}}^{h_{\Gamma_{b6}}}d_{\Gamma_{b6}}^{0}d_{\Gamma_{b6}}^{h_{\Gamma_{b6}}}e_{\Gamma_{b6}}^{n_{\Gamma_{b6}}}f_{\Gamma_{b6}}^{n_{\Gamma_{b6}}}\right]\left[c_{\Gamma_{c6}}^{h_{\Gamma_{c6}}}d_{\Gamma_{c6}}^{h_{\Gamma_{c6}}}e_{\Gamma_{c6}}^{n_{\Gamma_{c6}}}\right]\\&\left.\times\left[c_{\Gamma_7}^{h_{\Gamma_7}}\right]\right]^T\end{aligned} \tag{16}$$

$$[E]=[[E_{\Gamma_1}][E_{\Gamma_{a2}}][E_{\Gamma_{b2}}][E_{\Gamma_{c2}}][E_{\Gamma_3}][E_{\Gamma_{a4}}][E_{\Gamma_{b4}}][E_{\Gamma_{c4}}][E_{\Gamma_{d4}}][E_{\Gamma_{e4}}][E_{\Gamma_5}][E_{\Gamma_{a6}}][E_{\Gamma_{b6}}][E_{\Gamma_{c6}}][E_{\Gamma_7}]]^T \tag{17}$$

where $[E_{\Gamma_1}]$ to $[E_{\Gamma_7}]$ are the excitation current matrices for each region. The excitation current matrices in the region in contact with the transmitting coil, such as $[E_{\Gamma_3}]$, $[E_{\Gamma_{a4}}]$, $[E_{\Gamma_{b4}}]$, $[E_{\Gamma_{c4}}]$, $[E_{\Gamma_{d4}}]$, $[E_{\Gamma_{e4}}]$, and $[E_{\Gamma_5}]$ are not zero matrices. The rest are all zero matrices.

Equation (14) is simplified to (18). For the remaining regions similarly, Matrix $[T]$ can be expressed as (19) shown at the bottom of the next page. Matrix $[I]$ is the unit matrix.

$$d_{\Gamma_1}^{h_{\Gamma_1}}=\left[T_{\Gamma_1}^{\Gamma_{a2}}\right]+\left[T_{\Gamma_1}^{\Gamma_{b2}}\right]+\left[T_{\Gamma_1}^{\Gamma_{c2}}\right]. \tag{18}$$

III. Mutual Inductance Calculation for Rectangular Coils at Arbitrary Position Based on the VTCM Method

In the previous section, the magnetic vectors in the XZ-plane are known. A similar method is used to solve for the YZ-plane and then superimpose the two planes. Finally, the 3-D analytical result is obtained. Two planes of rectangular coils with bilateral finite magnetic shields at arbitrary position are shown in Fig. 5. The parameters in Fig. 5 are the same as those shown in Fig. 2. In Fig. 5(a), m is the distance of the horizontal misalignment of the receiving coil with the magnetic shielding on the receiving side. θ is the angle of the rotational misalignment of the receiving coil with the magnetic shield on the receiving side. The specific values of the parameters x and y are provided in the experimental section.

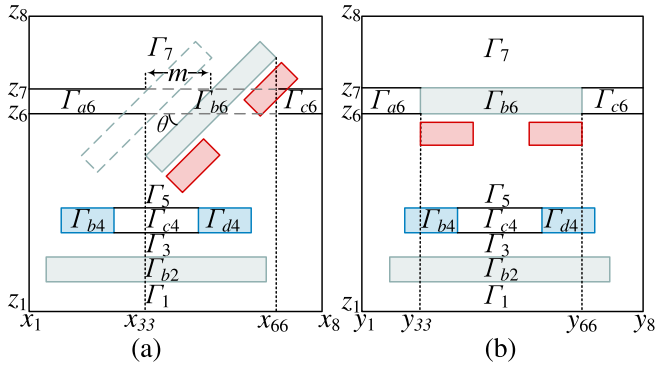

Fig. 5. Plan view of the rectangular coils with bilateral finite magnetic shields at arbitrary position.

As shown in Fig. 5(a), the magnetic shielding (Region Γ_{b6}) is horizontally and rotationally misaligned with the receiving coil at the same time. The projection of the magnetic shielding is performed by using the VCTM. The coordinates of the YZ-plane shown in Fig. 5(b) are maintained unchanged. The XZ-plane is divided into regions under the new coordinates according to the method of this article, and then the unknown coefficients are obtained. By using the VCTM, the new coordinates are obtained as follows:

$$\begin{bmatrix} x_{33} \\ x_{66} \end{bmatrix} = \begin{bmatrix} 1 & 0 & \frac{1}{2}(1-\cos(\theta)) \\ 0 & 1 & \frac{1}{2}(\cos(\theta)-1) \end{bmatrix} \begin{bmatrix} x_{33} \\ x_{66} \\ t_{x\Gamma_{b6}} \end{bmatrix} + \begin{bmatrix} m \\ m \end{bmatrix}. \quad (20)$$

The y-direction of the XZ-plane and the x-direction of the YZ-plane are finite. Therefore, a 3-D correction factor needs to be introduced. According to the ratio of an infinitely long conductor to a finite long conductor of the magnetic flux density in the Biot-Savart law, the correction factor for a parallel rectangular body in a certain plane can be obtained

$$f_{xz} = \frac{f_1}{f_2} = \frac{1}{2(g_1+g_2)} \cdot \left(\frac{g_2 g_4}{\sqrt{{g_1}^2+{g_4}^2}} - \frac{g_2 g_3}{\sqrt{{g_1}^2+{g_3}^2}} + \frac{g_1 g_4}{\sqrt{{g_2}^2+{g_4}^2}} - \frac{g_1 g_3}{\sqrt{{g_2}^2+{g_3}^2}} \right) \quad (21)$$

where f_1 is the infinitely long conductor flux and f_2 is the finite long conductor flux. g_1, g_2, g_3, and g_4 are expressed as follows:

$$g_1 = \sqrt{\left(x - \frac{1}{2}(x_3+x_4)\right)^2 + (z-(z_4+z_5))^2} \quad (22)$$

$$g_2 = \sqrt{\left(x - \frac{1}{2}(x_5+x_6)\right)^2 + (z-(z_4+z_5))^2} \quad (23)$$

$$\begin{cases} g_3 = (\frac{1}{2}(y_3+y_4) - y) \\ g_4 = (\frac{1}{2}(y_5+y_6) - y) \end{cases}. \quad (24)$$

To determine the effect of μ_r during the conversion from 2-D to 3-D, a factor $g(\mu_r)$ was proposed in the literature [25]. However, μ_r is only considered, and variations in the rectangular coil are not allowed at arbitrary position. For this purpose, a large number of curve fits was performed in this article, and the following functions are finally obtained:

$$Q(\mu_r, \theta, m) = g(\mu_r) \cdot \left(1 - 7.514 \cdot \left(\frac{\pi\theta}{180}\right)^{4.275} \cdot m\right). \quad (25)$$

$$[T] = \begin{bmatrix}
[I] & [T_{\Gamma_1}^{\Gamma_{a2}}] & [T_{\Gamma_1}^{\Gamma_{b2}}] & [T_{\Gamma_1}^{\Gamma_{c2}}] & [0] & [0] & [0] & [0] & [0] & [0] & [0] & [0] & [0] & [0] & [0] \\
[T_{\Gamma_{a2}}^{\Gamma_1}] & [I] & [T_{\Gamma_{a2}}^{\Gamma_{b2}}] & [0] & [T_{\Gamma_{a2}}^{\Gamma_3}] & [0] & [0] & [0] & [0] & [0] & [0] & [0] & [0] & [0] & [0] \\
[T_{\Gamma_{b2}}^{\Gamma_1}] & [T_{\Gamma_{b2}}^{\Gamma_{a2}}] & [I] & [T_{\Gamma_{b2}}^{\Gamma_{c2}}] & [T_{\Gamma_{b2}}^{\Gamma_3}] & [0] & [0] & [0] & [0] & [0] & [0] & [0] & [0] & [0] & [0] \\
[T_{\Gamma_{c2}}^{\Gamma_1}] & [0] & [T_{\Gamma_{c2}}^{\Gamma_{b2}}] & [I] & [T_{\Gamma_{c2}}^{\Gamma_3}] & [0] & [0] & [0] & [0] & [0] & [0] & [0] & [0] & [0] & [0] \\
[0] & [T_{\Gamma_3}^{\Gamma_{a2}}] & [T_{\Gamma_3}^{\Gamma_{b2}}] & [T_{\Gamma_3}^{\Gamma_{c2}}] & [I] & [T_{\Gamma_3}^{\Gamma_{a4}}] & [T_{\Gamma_3}^{\Gamma_{b4}}] & [T_{\Gamma_3}^{\Gamma_{c4}}] & [T_{\Gamma_3}^{\Gamma_{d4}}] & [T_{\Gamma_3}^{\Gamma_{e4}}] & [0] & [0] & [0] & [0] & [0] \\
[0] & [0] & [0] & [0] & [T_{\Gamma_{a4}}^{\Gamma_3}] & [I] & [T_{\Gamma_{a4}}^{\Gamma_{b4}}] & [0] & [0] & [0] & [T_{\Gamma_{a4}}^{\Gamma_5}] & [0] & [0] & [0] & [0] \\
[0] & [0] & [0] & [0] & [T_{\Gamma_{b4}}^{\Gamma_3}] & [T_{\Gamma_{b4}}^{\Gamma_{a4}}] & [I] & [T_{\Gamma_{b4}}^{\Gamma_{c4}}] & [0] & [0] & [T_{\Gamma_{b4}}^{\Gamma_5}] & [0] & [0] & [0] & [0] \\
[0] & [0] & [0] & [0] & [T_{\Gamma_{c4}}^{\Gamma_3}] & [0] & [T_{\Gamma_{c4}}^{\Gamma_{b4}}] & [I] & [T_{\Gamma_{c4}}^{\Gamma_{d4}}] & [0] & [T_{\Gamma_{c4}}^{\Gamma_5}] & [0] & [0] & [0] & [0] \\
[0] & [0] & [0] & [0] & [T_{\Gamma_{d4}}^{\Gamma_3}] & [0] & [0] & [T_{\Gamma_{d4}}^{\Gamma_{c4}}] & [I] & [T_{\Gamma_{d4}}^{\Gamma_{e4}}] & [T_{\Gamma_{d4}}^{\Gamma_5}] & [0] & [0] & [0] & [0] \\
[0] & [0] & [0] & [0] & [T_{\Gamma_{e4}}^{\Gamma_3}] & [0] & [0] & [0] & [T_{\Gamma_{e4}}^{\Gamma_{d4}}] & [I] & [T_{\Gamma_{e4}}^{\Gamma_5}] & [0] & [0] & [0] & [0] \\
[0] & [0] & [0] & [0] & [0] & [T_{\Gamma_5}^{\Gamma_{a4}}] & [T_{\Gamma_5}^{\Gamma_{b4}}] & [T_{\Gamma_5}^{\Gamma_{c4}}] & [T_{\Gamma_5}^{\Gamma_{d4}}] & [T_{\Gamma_5}^{\Gamma_{e4}}] & [I] & [T_{\Gamma_5}^{\Gamma_{a6}}] & [T_{\Gamma_5}^{\Gamma_{b6}}] & [T_{\Gamma_5}^{\Gamma_{c6}}] & [0] \\
[0] & [0] & [0] & [0] & [0] & [0] & [0] & [0] & [0] & [0] & [T_{\Gamma_{a6}}^{\Gamma_5}] & [I] & [T_{\Gamma_{a6}}^{\Gamma_{b6}}] & [0] & [T_{\Gamma_{a6}}^{\Gamma_7}] \\
[0] & [0] & [0] & [0] & [0] & [0] & [0] & [0] & [0] & [0] & [T_{\Gamma_{b6}}^{\Gamma_5}] & [T_{\Gamma_{b6}}^{\Gamma_{a6}}] & [I] & [T_{\Gamma_{b6}}^{\Gamma_{c6}}] & [T_{\Gamma_{b6}}^{\Gamma_7}] \\
[0] & [0] & [0] & [0] & [0] & [0] & [0] & [0] & [0] & [0] & [T_{\Gamma_{c6}}^{\Gamma_5}] & [0] & [T_{\Gamma_{c6}}^{\Gamma_{b6}}] & [I] & [T_{\Gamma_{c6}}^{\Gamma_7}] \\
[0] & [0] & [0] & [0] & [0] & [0] & [0] & [0] & [0] & [0] & [0] & [T_{\Gamma_7}^{\Gamma_{a6}}] & [T_{\Gamma_7}^{\Gamma_{b6}}] & [T_{\Gamma_7}^{\Gamma_{c6}}] & [I]
\end{bmatrix} \quad (19)$$

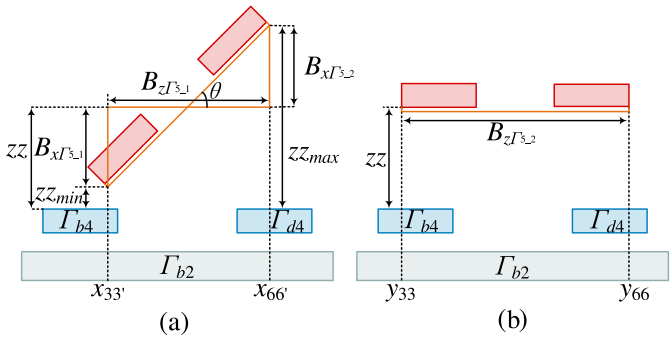

Fig. 6. Diagram of the receiving coil flux component.

Fig. 6 shows the 2-D model diagram with the magnetic shielding of the receiving coil neglected. According to the VCTM, the new coordinates of $x_{33'}$ and $x_{66'}$, $zz_{\min}$ and $zz_{\max}$ in the figure are as follows:

$$x_{33'} = x_{33} + \frac{1}{2}((x_{66} - t \cdot w) - (x_{33} + t \cdot w)) \cdot (1 - \cos(\theta)) + m \tag{26}$$

$$x_{66'} = x_{66} - \frac{1}{2}((x_{66} - t \cdot w) - (x_{33} + t \cdot w)) \cdot (1 - \cos(\theta)) + m \tag{27}$$

$$zz_{\min} = z_5 + zz - \frac{1}{2}((x_{66} - t \cdot w) - (x_{33} + t \cdot w)) \cdot \sin(\theta) \tag{28}$$

$$zz_{\max} = z_5 + zz + \frac{1}{2}((x_{66} - t \cdot w) - (x_{33} + t \cdot w)) \cdot \sin(\theta) \tag{29}$$

where $x_{33'} = y_{33'}$ and $x_{66'} = y_{66'}$.

The magnetic flux density at the receiving coil (Region Γ_5) is divided into several flux components, as shown in Fig. 6. According to (21) and (25) in the previous section, the expression for the magnetic flux density in Region Γ_5 in the 3-D model can be derived as follows:

$$B_5 = B_{x\Gamma_{5\_1}}(x,y,z) + B_{x\Gamma_{5\_2}}(x,y,z) + B_{z\Gamma_{5\_1}}(x,y,z) + B_{z\Gamma_{5\_2}}(x,y,z) \tag{30}$$

where $B_{x\Gamma_{5\_1}}(x,y,z)$, $B_{x\Gamma_{5\_2}}(x,y,z)$, and $B_{z\Gamma_{5\_1}}(x,y,z)$ are the 2-D model flux densities in the XZ-plane. $B_{z\Gamma_{5\_2}}(x,y,z)$ is the 2-D model flux densities in the YZ-plane. The expressions are as follows:

$$B_{x\Gamma_{5\_1}}(x,y,z) = B_{x\Gamma_{5\_2}}(x,y,z) = \frac{\partial A_{\Gamma_5}}{\partial z} \cdot f_{xz}(x,y,z) \cdot Q(\mu_r,\theta,m) \tag{31}$$

$$B_{z\Gamma_{5\_1}}(x,y,z) = B_{z\Gamma_{5\_2}}(x,y,z) = -\frac{\partial A_{\Gamma_5}}{\partial x} \cdot f_{yz}(x,y,z) \cdot Q(\mu_r,\theta,m). \tag{32}$$

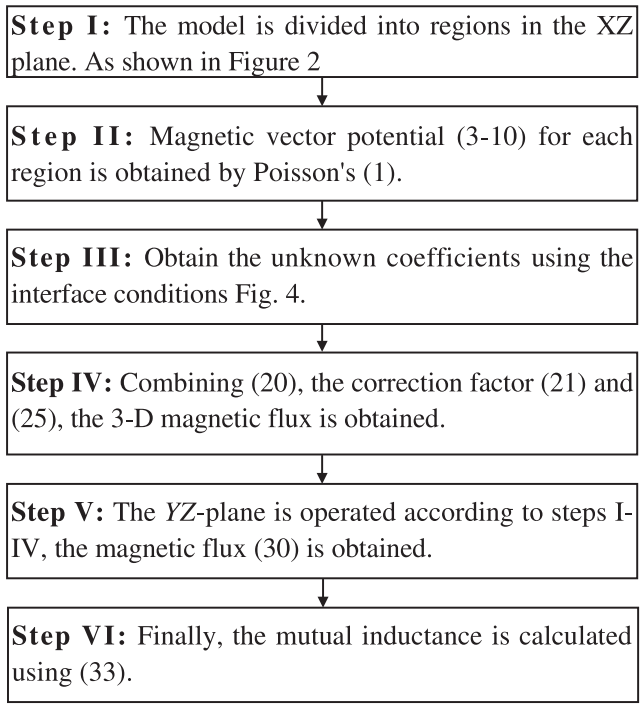

Fig. 7. Steps of for calculating the mutual inductance.

Finally, the mutual inductance expression of the proposed rectangular coils with bilateral finite magnetic shields at arbitrary position is as follows:

$$M = \frac{1}{I_p}\sum_{t=1}^{N_s}\left(\int_{x_{33'}+t\cdot w}^{x_{66'}-t\cdot w}\int_{y_{33}+t\cdot w}^{y_{66}-t\cdot w} B_{z\Gamma_{5\_1}}(x,y,z_5+zz)dxdy + \int_{x_{33'}+t\cdot w}^{x_{66'}-t\cdot w}\int_{y_{33}+t\cdot w}^{y_{66}-t\cdot w} B_{z\Gamma_{5\_2}}(x,y,z_5+zz)dxdy + \int_{y_{33'}+t\cdot w}^{y_{66'}-t\cdot w}\int_{z_5+zz}^{zz_{\min}} B_{x\Gamma_{5\_1}}(x_{33'}+t\cdot w,y,z)dydz + \int_{y_{33'}+t\cdot w}^{y_{66'}-t\cdot w}\int_{z_5+zz}^{zz_{\max}} B_{x\Gamma_{5\_2}}(x_{66'}-t\cdot w,y,z)dydz\right) \tag{33}$$

where N_s is the number of turns of the receiving coil.

The steps of mutual inductance calculation for the proposed analytical model are shown in Fig. 7.

IV. Verification of Experiments and Simulations

To verify the feasibility of the arbitrary position during the mutual inductance calculation proposed in this article, a set of transceiver coil devices is built, as shown in Fig. 8. The detailed parameters of the coil and magnetic shielding are shown in Table I. The experimental environment is used with a 24-core Intel processor with 2.2-GHz clock frequency and 64 GB RAM. The programming tool is MATLAB. Number of elements in each FEM simulation is: 63440-93031.

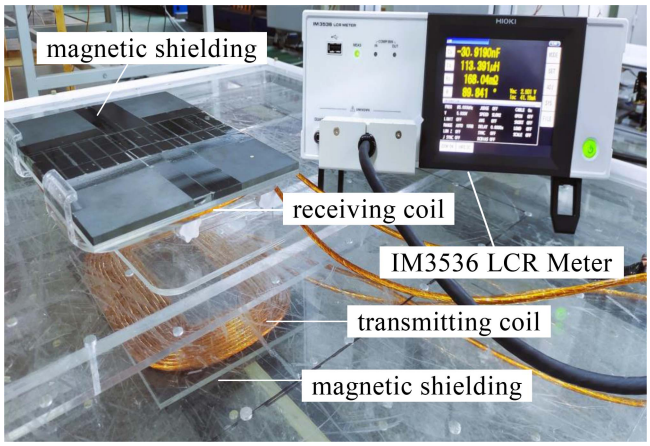

Fig. 8. Diagram of the experimental setup.

TABLE I
PARAMETERS OF THE COIL AND MAGNETIC SUBSTRATE

Parameter	Value
Number of turns of the transmitting coil, N_p	13
Number of turns of receiving coil, N_s	14
Diameter of copper wire, w	5 mm
Air gap between coil and magnetic shielding, b	5 mm
Thickness of magnetic shielding, d	5 mm
Relative permeability of magnetic shielding, μ_r	2800
Excitation current of the transmitting coil, I_p	10 A
Frequency of current	85 kHz
Harmonics ($H_{\Gamma a2}$, $H_{\Gamma b2}$, $H_{\Gamma c2}$, $H_{\Gamma a6}$, $H_{\Gamma b6}$, $H_{\Gamma c6}$, $N_{\Gamma a2}$, $N_{\Gamma b2}$, $N_{\Gamma c2}$, $N_{\Gamma a6}$, $N_{\Gamma b6}$, $N_{\Gamma c6}$)	50
Harmonics ($H_{\Gamma a4}$, $H_{\Gamma b4}$, $H_{\Gamma c4}$, $H_{\Gamma d4}$, $H_{\Gamma e4}$, $N_{\Gamma a4}$, $N_{\Gamma b4}$, $N_{\Gamma c4}$, $N_{\Gamma d4}$, $N_{\Gamma e4}$)	100
Harmonics for ($H_{\Gamma 1}$, $H_{\Gamma 3}$, $H_{\Gamma 5}$, $H_{\Gamma 7}$)	150
Parameter (x_1, x_2, x_3, x_{33}, x_4, x_5, x_6, x_{66}, x_7, x_8)	(0, 1, 1, 1.012, 1.077, 1.247,1.312, 1.324, 1.324, 2.324) m
Parameter (y_1, y_2, y_3, y_{33}, y_4, y_5, y_6, y_{66}, y_7, y_8)	(0, 1, 1, 1, 1.065, 1.135,1.2, 1.2, 1.2, 2.2) m
Parameter (z_1, z_2, z_3, z_4, z_5)	(-1.015, -0.015, -0.01, -0.005, 0) m
Coil length in the x-direction ($x_{66} - x_{33}$)	312 mm
Coil length in the y-direction ($y_{66} - y_{33}$)	200 mm

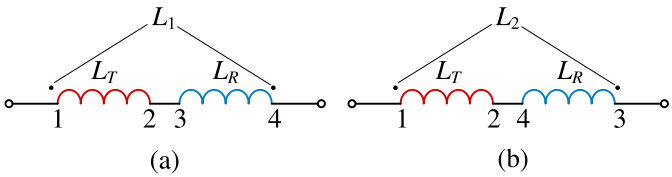

Fig. 9. Experimental connection diagram of coil mutual inductance. (a) Coserial connection. (b) Antiserial connection.

In this article, an IM 3536 *LCR* impedance analyzer is used for measurement. The mutual inductance is measured as follows: 1) As shown in Fig. 9(a), the transmitting and receiving coils are connected in series in the same phase, and the measured inductance is $L_1 = L_T + L_R + 2\,M$; 2) As shown in Fig. 9(b), the transmitting and receiving coils are connected in series in the opposite phase, and the measured inductance is $L_2 = L_T + L_R - 2\,M$. Then, the mutual inductance between the transmitting and receiving coils is $M = \mid L_1 - L_2 \mid /4$, where L_T is the self-inductance of transmitting coil and L_R is the self-inductance of receiving coil.

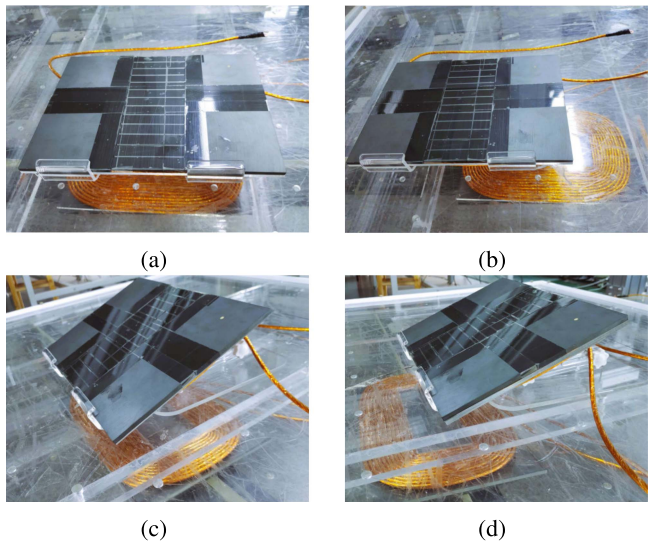

Fig. 10. Experimental model of the coil position variation. (a) Vertical misalignment. (b) Horizontal misalignment. (c) Rotational misalignment. (d) Horizontal and rotational misalignment.

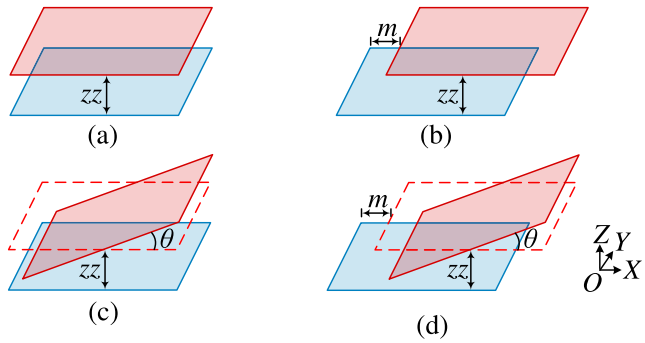

Fig. 11. Simplified diagram of bilateral model. (a) Vertical misalignment. (b) Horizontal misalignment. (c) Rotational misalignment. (d) Horizontal and rotational misalignment.

The simulation was verified by using the 3-D finite element tool Ansys Maxwell, and the experimental model is shown in Fig. 10. Experiments and simulations were conducted for four cases of vertical misalignment, horizontal misalignment, rotational misalignment, and horizontal and rotational misalignment. The simulated results, experimental measurements, and calculated results of the mutual inductance are compared.

Fig. 11 shows a simplified model. The magnetic shielding and the coil are considered as a whole. The experiment will be performed as shown in the figure below. Where ε_1 is the simulation error, and ε_2 is the experimental error. The expressions are as follows:

$$\varepsilon_1 = |M_c - M_s|/M_s \tag{34}$$

$$\varepsilon_2 = |M_c - M_e|/M_e \tag{35}$$

TABLE II
MUTUAL INDUCTANCE FOR VERTICAL MISALIGNMENT

zz(mm)	M_s(μH)	M_e(μH)	M_c(μH)	ε_1	ε_2
40	39.8005	39.8894	40.8022	2.52%	2.29%
50	32.5209	33.2859	33.2251	2.17%	0.18%
60	26.9547	27.2892	27.2973	1.27%	0.03%
70	22.5695	22.6673	22.5962	0.12%	0.31%
80	19.0255	18.9088	18.8294	1.03%	0.42%
90	16.1975	15.9346	15.7872	2.53%	0.93%
100	13.8486	13.4825	13.3131	3.87%	1.26%
110	11.8988	11.5043	11.4964	3.38%	0.07%
120	10.2917	9.8483	10.2733	0.18%	4.32%
130	8.9531	8.5045	8.7863	1.86%	3.31%
140	7.8117	7.3708	7.5508	3.34%	2.44%

TABLE III
MUTUAL INDUCTANCE FOR HORIZONTAL MISALIGNMENT

m(mm)	M_s(μH)	M_e(μH)	M_c(μH)	ε_1	ε_2
-100	7.6362	7.5541	7.6892	0.69%	1.79%
-80	8.9945	8.6941	8.9155	0.88%	2.55%
-60	10.1863	9.9105	10.0375	1.46%	1.28%
-40	11.1324	10.8128	10.9541	1.60%	1.31%
-20	11.7407	11.3723	11.5601	1.54%	1.65%
0	11.8988	11.5051	11.7734	1.05%	2.33%
20	11.6434	11.1558	11.5601	0.72%	3.62%
40	10.9482	10.7763	10.9541	0.05%	1.65%
60	9.9209	9.8443	10.0375	1.18%	1.96%
80	8.7568	8.7228	8.9155	1.81%	2.21%
100	7.5748	7.5535	7.6892	1.51%	1.80%

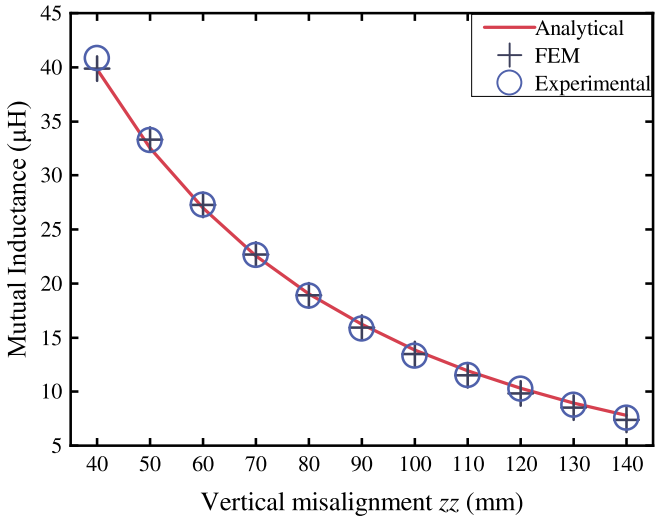

Fig. 12. Diagram of the experimental results for vertical misalignment.

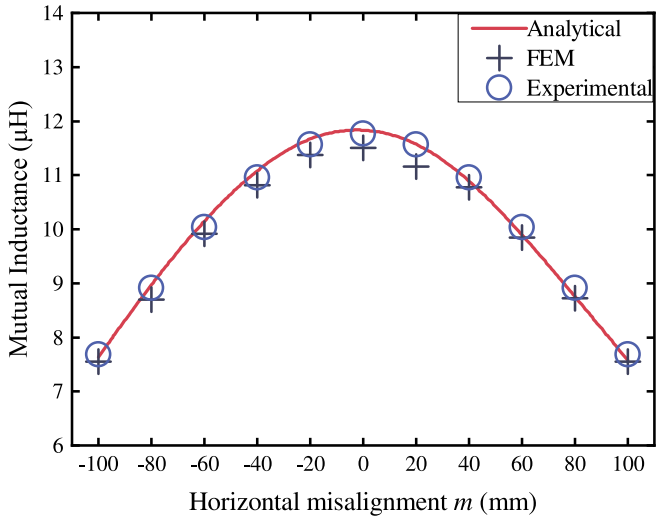

Fig. 13. Diagram of the experimental results for horizontal misalignment.

where M_c is the mutual inductance calculation result, M_s is the mutual inductance simulation result, and M_e is the actual mutual inductance measurement result.

A. Vertical Misalignment

The position change diagram of the vertical misalignment is shown in Fig. 11(a). zz denotes the air gap from the transmitting coil to the receiving coil. The range of zz is 40–140 mm, and the step length is set to 10 mm. The results and errors of the calculated, simulated, and experimental results of mutual inductance are shown in Table II.

According to the data in Table II, ε_1 is less than 3.87%, and ε_2 is less than 4.32%. The results show that the calculated, simulated, and experimentally measured results match. According to the data in Table II, the coil mutual inductance variation curve under vertical misalignment is plotted in Fig. 12.

As shown in Fig. 12, when the air gap between the transmitting coil and the receiving coil is misaligned by the minimum amount of zz, the mutual inductance achieves the maximum value. As the air gap increases, the mutual inductance gradually decreases. This is because the coupling between the coils decreases with an increasing air gap.

B. Horizontal Misalignment

The position change of the horizontal misalignment is shown in Fig. 11(b). m indicates the distance of the horizontal misalignment between the transmitting coil and the receiving coil. zz has an initial value of 110 mm. m is set to an initial value of 0 mm and a step size of ±20 mm. The results and errors of the calculated, simulated, and experimental results of the mutual inductance are shown in Table III.

In Table III, ε_1 is less than 1.81%, and ε_2 is less than 3.62%. The results show that the calculated, simulated, and experimental measurement results match. According to the data in Table III, the coil mutual inductance variation curve under horizontal misalignment is plotted in Fig. 13.

As shown in Fig. 13, when the horizontal misalignment between the transmitting coil and the receiving coil m is smallest, the mutual inductance achieves the maximum value. As the horizontal misalignment increases, the mutual inductance decreases. This is because the coupling area between the receiving coil and the transmitting coil decreases, which leads to a rapid decrease in the mutual inductance.

TABLE IV
MUTUAL INDUCTANCE FOR ROTATIONAL MISALIGNMENT

$\theta(^\circ)$	$M_s(\mu H)$	$M_e(\mu H)$	$M_c(\mu H)$	ε_1	ε_2
-50	11.8817	11.7345	11.3293	4.65%	3.45%
-40	13.3461	13.2135	12.7071	4.79%	3.83%
-30	13.2076	13.1331	12.9055	2.29%	1.73%
-20	12.5542	12.3321	12.5822	0.22%	2.03%
-10	12.0817	12.0576	12.1453	0.53%	0.73%
0	11.8988	11.5051	11.7731	1.06%	2.33%
10	12.0322	12.0595	12.1453	0.94%	0.71%
20	12.4551	12.3265	12.5822	1.02%	2.07%
30	13.0277	13.0021	12.9055	0.94%	0.74%
40	13.2089	13.0615	12.7071	3.80%	2.71%
50	11.6338	11.6005	11.3293	2.62%	2.34%

TABLE V
MUTUAL INDUCTANCE FOR HORIZONTAL AND ROTATIONAL MISALIGNMENT

m(mm)	$M_s(\mu H)$	$M_e(\mu H)$	$M_c(\mu H)$	ε_1	ε_2
-100	7.8409	7.6843	7.8985	0.73%	2.79%
-80	9.5193	9.4403	9.6602	1.48%	2.33%
-60	11.1529	10.9621	11.2932	1.26%	3.02%
-40	12.4901	12.3735	12.6273	1.10%	2.05%
-20	13.1786	13.0948	13.3191	1.07%	1.71%
0	13.0277	13.0021	13.2845	1.97%	2.17%
20	12.2014	12.2428	12.4612	2.13%	1.78%
40	10.9029	11.1195	11.0653	1.49%	0.49%
60	9.4239	9.5763	9.3827	0.44%	2.02%
80	7.8162	7.9093	7.6424	2.22%	3.37%
100	6.1583	6.1955	5.9589	3.24%	3.82%

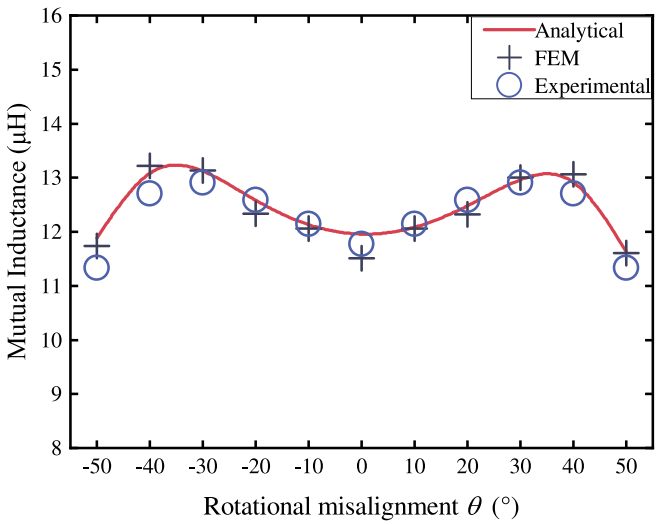

Fig. 14. Diagram of the experimental results for rotational misalignment.

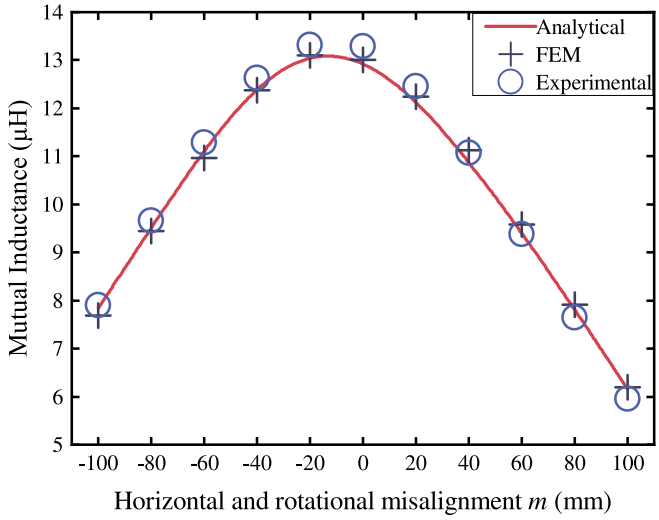

Fig. 15. Diagram of the experimental results for horizontal and rotational misalignment.

C. Rotational Misalignment

The position change diagram of the rotational misalignment is shown in Fig. 11(c). θ indicates the rotation angle of the receiving coil and the receiving side magnetic shielding around the Y-axis simultaneously. zz has an initial value of 110 mm. θ is set to an initial value of 0° with a step size of $\pm 10^\circ$. The results and errors of the calculated, simulated, and experimental values of the mutual inductance are shown in Table IV.

According to the data in Table IV, ε_1 is less than 4.79%, and ε_2 is less than 3.83%. The results show that the calculated, simulated, and experimental measurement results match. The mutual inductance change curve under rotational misalignment is plotted in Fig. 14.

Fig. 14 shows that the mutual inductance increases and then decreases when the receiving coil and the magnetic shielding are rotated around the Y-axis at the same time.

D. Horizontal and Rotational Misalignment

The position change diagram of the horizontal and rotational misalignment is shown in Fig. 11(d). zz has an initial value of 110 mm, and θ has an initial value of 30°. The horizontal misalignment m is from -100 to $+100$ mm in steps of ± 20 mm. The results and errors of the calculated, simulated, and experimental results of the mutual inductance are shown in Table V.

According to the data in Table V, ε_1 is less than 3.24%, and ε_2 is less than 3.82%. The results show that the calculated, simulated, and experimental measurements match. The coil mutual inductance change curve under horizontal and rotational misalignment is plotted in Fig. 15. As shown in Fig. 15, when the rotation misalignment θ is 30° and the horizontal misalignment m is -20 mm, the mutual inductance achieves the maximum value.

E. Effect of Harmonic Number

In order to research the effect of harmonic number on the calculation accuracy and calculation time, the harmonic number is divided into three groups: 1) the region where the magnetic shielding is located ($\Gamma_{a2}, \Gamma_{b2}, \Gamma_{c2}, \Gamma_{a6}, \Gamma_{b6}, \Gamma_{c6}$); 2) the region where the transmitting coils are located ($\Gamma_{a4}, \Gamma_{b4}, \Gamma_{c4}, \Gamma_{d4}, \Gamma_{e4}$); and 3) the all-air region ($\Gamma_1, \Gamma_3, \Gamma_5, \Gamma_7$). Each set of experiments is categorized into two cases of vertical misalignment and arbitrary position: 1) Set vertical misalignment $zz = 110$ mm, horizontal misalignment $m = 0$ mm, and rotational misalignment

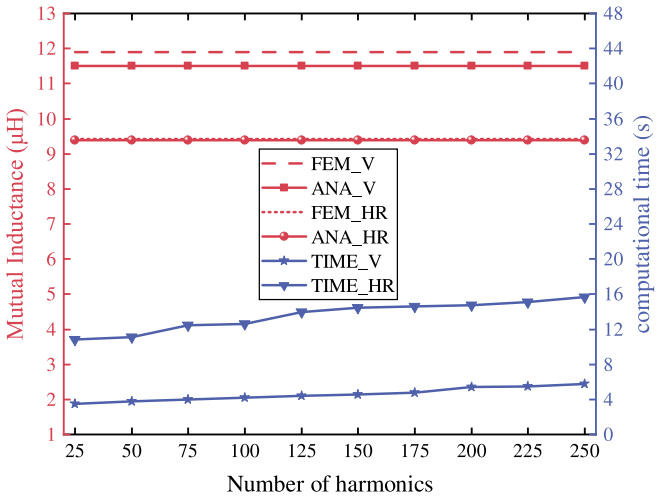

Fig. 16. Diagram of boundary conditions. (a) Regions Γ_{a2}, Γ_{b2}, Γ_{c2}, Γ_{a6}, Γ_{b6}, and Γ_{c6}.

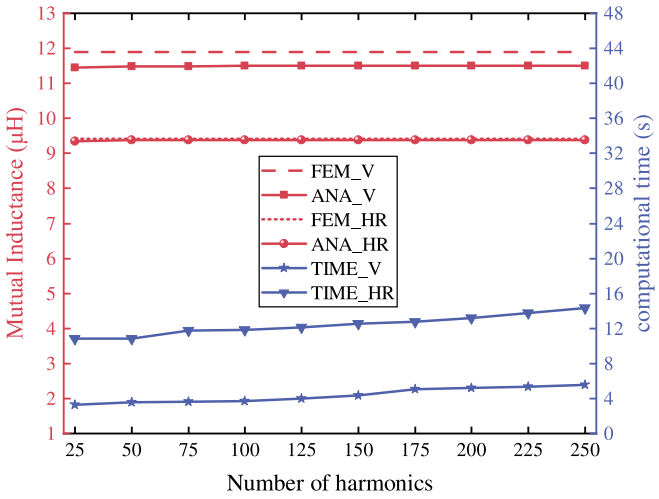

Fig. 17. Diagram of boundary conditions. (b) Regions Γ_{a4}, Γ_{b4}, Γ_{c4}, Γ_{d4}, and Γ_{e4}.

$\theta = 0°$. 2) Set vertical misalignment $zz = 110$ mm, horizontal misalignment $m = 60$ mm, and rotational misalignment $\theta = 30°$. The number of harmonics is from 25 to 250 in steps of 25. Using the simulated values as a reference, the effect of the number of harmonics on the accuracy and calculation time is shown below.

As shown in Fig. 16, the highest accuracy of mutual inductance calculation is obtained when the number of harmonics is equal to 50. From Fig. 17, the highest accuracy of mutual inductance calculation is obtained when the number of harmonics is equal to 100. And then when the number of harmonics continues to increase, the mutual inductance calculation accuracy remains unchanged, but the calculation time increases.

In Figs. 16–18, FEM_V and ANA_V denote the simulated and calculated results at vertical misalignment, respectively, FEM_HR and ANA_HR denote the simulated and calculated results at arbitrary position, respectively, and TIME_V and TIME_HR denote the runtime of the procedure at vertical misalignment and arbitrary position, respectively.

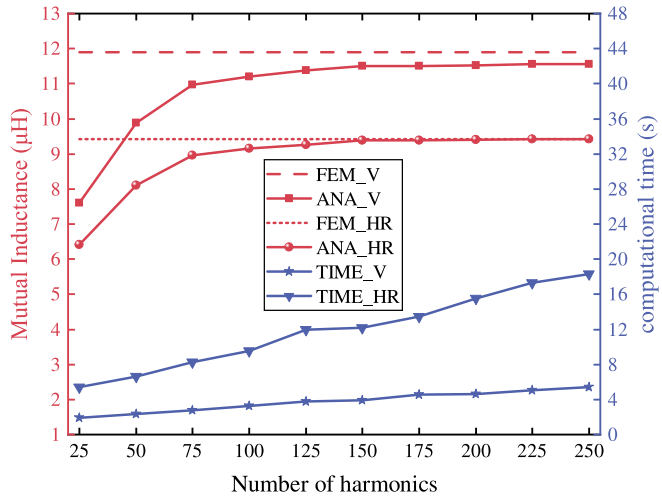

Fig. 18. Diagram of boundary conditions. (c) Regions Γ_1, Γ_3, Γ_5, and Γ_7.

TABLE VI
TIME COMPARISON OF THE CALCULATED AND SIMULATED RESULTS

Modeling Type	RA (s)	RF (s)
vertical misalignment	4	75
horizontal misalignment	12	79
rotational misalignment	12	132
horizontal and rotational misalignment	12	129

where RA is the runtime of analytic and RF is the runtime of 422 FEM.

As shown in Fig. 18, the mutual inductance calculation accuracy is higher with the increase of the harmonic number and stabilizes at 150. However, when the harmonic number is larger than 150, the computation time continues to increase. Because the receiving coil is located in region Γ_5, the accuracy of the mutual inductance calculation will decrease when a harmonic number is too small; whereas the computation time will increase when a harmonic number is too large.

F. Comparison

In this section, the runtime of the proposed calculation method is compared with the runtime of FEM, as shown in Table VI. The runtime of the proposed method is approximately 4 s with vertical misalignment, which is approximately 19 times faster than that of the FEM. The runtime of other three misalignments is 12 s, which is approximately 11 times faster than that of the FEM, verifying the rapidity of the method. More importantly, the runtime of the proposed method does not increase with the scale of the model, but the runtime of the FEM increases significantly with the scale of the model.

The proposed method of this article is compared with other methods in the literature mentioned in Table VII. Table VII shows that the proposed method has a high degree of freedom in receiving coils with a complex computational model and a small error rate. The feasibility and superiority of the proposed method is verified in this article.

TABLE VII
COMPARISON OF THE METHODS AMONG IN THIS PAPER AND OTHER LITERATURE

Literature	Method	HM	AP	SM	BM	FT	FL	ER
[18]	Biot-Savart	✗	✗	✗	✗	✗	✗	5.84%
[19]	SOVP formulation	✓	✗	✗	✗	✗	✗	3.00%
[20]	Vertex method	✓	✗	✗	✗	✗	✗	5.00%
[21]	Stokes Theorem	✓	✓	✗	✗	✗	✗	4.33%
[22]	Hyperbolic function	✓	✓	✗	✗	✗	✗	5.00%
[23]	Bessel transformation	✓	✗	✓	✗	✗	✗	8.57%
[24]	Fourier series	✓	✓	✓	✗	✓	✗	7.30%
[26]	Separate variable	✓	✗	✓	✓	✓	✓	14.50%
This paper	SPM, VCTM	✓	✓	✓	✓	✓	✓	4.79%

where HM is the horizontal misalignment.
AP is the arbitrary position.
SM is the single-side magnetic shielding.
BM is the bilateral magnetic shields.
FT is the finite thickness of the magnetic shielding.
FL is the finite length of the magnetic shielding.
ER is the maximum error rate.

V. CONCLUSION

In this article, a mutual inductance calculation method for rectangular coils with bilateral finite magnetic shields at arbitrary position is proposed. First, the 3-D rectangular coil structure is analyzed into two 2-D planes. The mutual inductance calculation formula is derived for rectangular coils with bilateral finite magnetic shields at vertical misalignment using the SPM. Second, a VCTM is proposed for the case of horizontal and rotational misalignment between the coils, and the mutual inductance expression is obtained for the rectangular coils at arbitrary position. The experimental results show that the mutual inductance calculation, simulation, and experimental results are basically consistent. The maximum error does not exceed 4.79%, and the computation time of the proposed method is about 11 times of the simulation time. Compared with finite element simulation, the proposed method is capable of model parameterization, and the parameters can be flexibly modified according to the requirements. The proposed method not only provides a theoretical basis for the fast optimization of mutual inductance between coils in wireless charging systems for electric vehicles, but also provides a theoretical basis for the next study of mutual inductance calculation methods between rectangular coils with bilateral toroidal magnetic shields at arbitrary locations.

REFERENCES

[1] Y. Chen et al., "A clamp circuit-based inductive power transfer system with reconfigurable rectifier tolerating extensive coupling variations," *IEEE Trans. Power Electron.*, vol. 39, no. 2, pp. 1942–1946, Feb. 2024.

[2] R. Qin, J. Li, J. Sun, and D. Costinett, "Shielding design for high-frequency wireless power transfer system for EV charging with self-resonant coils," *IEEE Trans. Power Electron.*, vol. 38, no. 6, pp. 7900–7909, Jun. 2023.

[3] H. Zhuang, W. Wang, and G. Yan, "Ferrite concentrating and shielding structure design of wireless power transmitting coil for inductively coupled capsule robot," *IEEE Trans. Biomed. Circuits Syst.*, vol. 17, no. 1, pp. 45–53, Feb. 2023.

[4] J. Ahn et al., "An out-of-phase wireless power transfer system for implantable medical devices to reduce human exposure to electromagnetic field and increase power transfer efficiency," *IEEE Trans. Biomed. Circuits Syst.*, vol. 16, no. 6, pp. 1166–1180, Dec. 2022.

[5] J.-Q. Zhu, Y.-L. Ban, R.-M. Xu, and C. C. Mi, "An NFC-connected coupler using IPT-CPT-combined wireless charging for metal-cover smartphone applications," *IEEE Trans. Power Electron.*, vol. 36, no. 6, pp. 6323–6338, Jun. 2021.

[6] W. Tang, Q. Zhu, J. Yang, D. Song, M. Su, and R. Zou, "Simultaneous 3-D wireless power transfer to multiple moving devices with different power demands," *IEEE Trans. Power Electron.*, vol. 35, no. 5, pp. 4533–4546, May 2020.

[7] Z. Zhang, S. Shen, Z. Liang, S. H. K. Eder, and R. Kennel, "Dynamic-balancing robust current control for wireless drone-in-flight charging," *IEEE Trans. Power Electron.*, vol. 37, no. 3, pp. 3626–3635, Mar. 2022.

[8] J. M. Arteaga, S. Aldhaher, G. Kkelis, C. Kwan, D. C. Yates, and P. D. Mitcheson, "Dynamic capabilities of multi-mHz inductive power transfer systems demonstrated with batteryless drones," *IEEE Trans. Power Electron.*, vol. 34, no. 6, pp. 5093–5104, Jun. 2019.

[9] Z. Zhang, A. Georgiadis, and C. Cecati, "Wireless power transfer for smart industrial and home applications," *IEEE Trans. Ind. Electron.*, vol. 66, no. 5, pp. 3959–3962, May 2019.

[10] Z. Li, J. Li, S. Li, Y. Yu, and J. Yi, "Design and optimization of asymmetric and reverse series coil structure for obtaining quasi-constant mutual inductance in dynamic wireless charging system for electric vehicles," *IEEE Trans. Veh. Technol.*, vol. 71, no. 3, pp. 2560–2572, Mar. 2022.

[11] J. Yi, P. Yang, Z. Li, P. Kong, and J. Li, "Mutual inductance calculation of circular coils for an arbitrary position with a finite magnetic core in wireless power transfer systems," *IEEE Trans. Transport. Electrific.*, vol. 9, no. 1, pp. 1950–1959, Mar. 2023.

[12] X. Zhang, C. Quan, and Z. Li, "Mutual inductance calculation of circular coils for an arbitrary position with electromagnetic shielding in wireless power transfer systems," *IEEE Trans. Transport. Electrific.*, vol. 7, no. 3, pp. 1196–1204, Sep. 2021.

[13] J. Acero, C. Carretero, I. Lope, R. Alonso, O. Lucia, and J. M. Burdio, "Analysis of the mutual inductance of planar-lumped inductive power transfer systems," *IEEE Trans. Ind. Electron.*, vol. 60, no. 1, pp. 410–420, Jan. 2013.

[14] S. Babic, F. Sirois, C. Akyel, G. Lemarquand, V. Lemarquand, and R. Ravaud, "New formulas for mutual inductance and axial magnetic force between a thin wall solenoid and a thick circular coil of rectangular cross-section," *IEEE Trans. Magn.*, vol. 47, no. 8, pp. 2034–2044, Aug. 2011.

[15] R. Ravaud, G. Lemarquand, S. Babic, V. Lemarquand, and C. Akyel, "Cylindrical magnets and coils: Fields, forces, and inductances," *IEEE Trans. Magn.*, vol. 46, no. 9, pp. 3585–3590, Sep. 2010.

[16] R. Oliveira and P. Lehn, "An improved mutual inductance electromagnetic model for inductive power transfer systems under misalignment conditions," *IEEE Trans. Veh. Technol.*, vol. 69, no. 6, pp. 6079–6093, Jun. 2020.

[17] Y. Cheng and Y. Shu, "A new analytical calculation of the mutual inductance of the coaxial spiral rectangular coils," *IEEE Trans. Magn.*, vol. 50, no. 4, Apr. 2014, Art. no. 7026806.

[18] E. Aydin, E. Yildiriz, and M. T. Aydemir, "A new semi-analytical approach for self and mutual inductance calculation of hexagonal spiral coil used in wireless power transfer systems," *Elect. Eng.*, vol. 103, no. 3, pp. 1769–1778, Jan. 2021.

[19] W. Dehui, S. Qisheng, W. Xiaohong, and H. Tianfu, "Analytical calculation of mutual coupling between two misaligned rectangular coils with rectangular cross-section in wireless power applications," *J. Phys. D: Appl. Phys.*, vol. 50, no. 43, Oct. 2017, Art. no. 43LT06.

[20] W. Dehui, S. Qisheng, W. Xiaohong, and Y. Fan, "Analytical model of mutual coupling between rectangular spiral coils with lateral misalignment for wireless power applications," *IET Power Electron.*, vol. 11, no. 5, pp. 781–786, Feb. 2018.

[21] H. Altun and N. Pirinççi, "A novel analytical model for mutual inductance calculations between two non-identical n-sided polygonal planar coils arbitrarily positioned in 3-D space for wireless power transfer," *IEEE Trans. Power Electron.*, vol. 38, no. 8, pp. 10396–10411, Aug. 2023.

[22] D. Wu, F. Cheng, and C. Huang, "Analytical computation of mutual inductance between two rectangular spiral coils with misalignments for wireless power applications," *Microw. Opt. Technol. Lett.*, vol. 62, no. 2, pp. 637–642, Oct. 2020.

[23] Z. Luo and X. Wei, "Analysis of square and circular planar spiral coils in wireless power transfer system for electric vehicles," *IEEE Trans. Ind. Electron.*, vol. 65, no. 1, pp. 331–341, Jan. 2018.

[24] B. K. Kushwaha, G. Rituraj, and P. Kumar, "3-D analytical model for computation of mutual inductance for different misalignments with shielding in wireless power transfer system," *IEEE Trans. Transport. Electrific.*, vol. 3, no. 2, pp. 332–342, Jun. 2017.

[25] G. Rituraj, B. K. Kushwaha, and P. Kumar, "A subdomain analytical model of coil system with magnetic shields of finite dimensions and finite permeability for wireless power transfer systems," *IEEE Trans. Magn.*, vol. 56, no. 12, Dec. 2020, Art. no. 8400511.
[26] Z. Luo, S. Nie, M. Pathmanathan, W. Han, and P. W. Lehn, "3-D analytical model of bipolar coils with multiple finite magnetic shields for wireless electric vehicle charging systems," *IEEE Trans. Ind. Electron.*, vol. 69, no. 8, pp. 8231–8242, Aug. 2022.
[27] F. Dubas and K. Boughrara, "New scientific contribution on the 2-D subdomain technique in cartesian coordinates: Taking into account of iron parts," *Math. Comput. Appl.*, vol. 22, no. 1, Feb. 2017, Art. no. 17.
[28] F. Dubas and A. Rahideh, "Two-dimensional analytical permanent-magnet eddy-current loss calculations in slotless PMSM equipped with surface-inset magnets," *IEEE Trans. Magn.*, vol. 50, no. 3, pp. 54–73, Mar. 2014.

Zhongbang Chen was born in China in 1999. He received the bachelor's degree in automation from Software Engineering Institute of GuangZhou, GuangZhou, China, in 2017. He is currently working toward the master's degree in control theory and control engineering with Hunan University of Technology, Zhuzhou, China.

His current research interests include wireless power transfer systems.

Zhongqi Li (Member, IEEE) was born in China in 1985. He received the M.Sc. degree in electrical engineering from Hunan University of Technology, Zhuzhou, China in 2012, and the Ph.D. degree in electrical engineering from the Hunan University, Changsha, China, in 2016.

From 2016, he is currently working as an Assistant Professor with Hunan University of Technology, Zhuzhou, China. From 2020, he is currently working as a Postdoctoral Fellow with Hunan University, Changsha, China. His research interests include wireless power transfer systems and soft-switching power converters.

Zhiyuan Lin was born in China in 1996. He received the bachelor's degree in electronic information engineering from HuBei University of Technology Engineering and Technology College, WuHan, China, in 2015. He is currently working toward the master's degree in electronic information with Hunan University of Technology, Zhuzhou, China.

His current research interests include wireless power transfer systems.

Junjun Li was born in Yichun, Jiangxi, China, in 1976. He received the B.Sc., M.Sc., and Ph.D. degrees in electrical engineering from Hunan University, Changsha, China, in 1999, 2004, and 2011, respectively.

From 2013 to 2017, he had conducted postdoctoral research with the CRRC Zhuzhou Institute Co., Ltd., Zhuzhou, China. He is currently an Instructor with the College of Traffic Engineering, Hunan University of Technology, Zhuzhou, China. His current research interests include the application of power electronics technology in new energy sources and new energy vehicles.

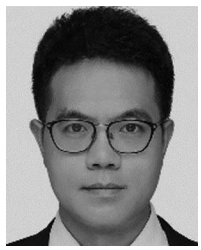

Yiming Zhang (Senior Member, IEEE) received the B.S. and Ph.D. degrees in electrical engineering from Tsinghua University, Beijing, China, in 2011 and 2016, respectively.

Afterward, he was a postdoctoral Researcher with San Diego State University, San Diego, CA, USA and a Research Fellow with Nanyang Technological University, Singapore. He is currently a Full Professor with Fuzhou University. He has authored 1 book from Springer, authored or co-authored more than 70 technical papers in journals and conference proceedings. His research interests include wireless power transfer for electric vehicles and mobile phones, and resonant converters.

Dr. Zhang was the recipient of the Outstanding Doctoral Dissertations of Tsinghua University in 2016. He was recognized as an Outstanding Reviewer for IEEE TRANSACTIONS ON POWER ELECTRONICS in 2019 and a Distinguished Reviewer for IEEE TRANSACTIONS ON INDUSTRIAL ELECTRONICS in 2020. He was a Topic Chair for IEEE Transportation Electrification Conference and Expo (ITEC) in 2018.